Supplementary information: Cross-hatch strain effects on SiGe quantum dots for qubit variability estimation

Luis Fabián Peña,[1] Mitchell I. Brickson,[2] Fabrizio Rovaris,[3] J. Houston Dycus,[4] Anthony McDonald,[1] Zachary T. Piontkowski,[1] Joel Benjamin Ruzindana,[5] Adelaide M. Bradicich,[6] Don Bethke,[6] Robin Scott,[7] Thomas E. Beechem,[8] Francesco Montalenti,[3] N. Tobias Jacobson,[2,*] and Ezra Bussmann[1,†]

[1]*Sandia National Laboratories, Albuquerque NM, USA*[‡]
[2]*Center for Computing Research, Sandia National Laboratories, Albuquerque NM, USA*
[3]*Department of Materials Science, University of Milano-Bicocca, Milano, Italy*
[4]*Advanced Microscopy, Eurofins EAG Materials Science, Raleigh NC, USA*
[5]*Department of Chemistry and Physics, University of Arkansas at Pine Bluff, Pine Bluff AR, USA*
[6]*Center for Integrated Nanotechnologies, Sandia National Laboratories, Albuquerque NM, USA*
[7]*Lawrence Semiconductor Research Laboratory, Inc., Tempe AZ, USA*
[8]*Mechanical Engineering and Birck Nanotechnology Center, Purdue University, West Lafayette IN, USA*
(Dated: January 20, 2026)

I. SUPPLEMENTARY METHODS - GROWTH STUDY

The growth study tracked surface evolution of 25 wafers undergoing a standard commercial chemical vapor deposition process, with details covered in the Methods. Table I indicates the layer stacks and growth temperatures prepared for this study. Table II indicates the growth rates across the wafer set.

TABLE S1. Growth study tracking growth surface morphology and strain evolution of 25 wafers through steps in a standard commercial CVD process

Wafer	Process	Characterization
1, 2	Si(100) substrate	STM
3, 4	Graded layer + relaxed buffer	AFM
5, 6	CMP of virtual substrate	AFM
7	LSRL Prep	AFM
8	T = 600 °C, SiGe regrowth 5 nm	AFM
9	T = 600 °C, SiGe regrowth 70 nm	AFM
10	T = 600 °C, SiGe regrowth 70 nm/ well 10 nm	AFM
11	T = 600 °C, SiGe regrowth 70 nm/ well 10 nm/ SiGe 50 nm/ Si cap 3 nm	AFM
12	T = 600 °C, SiGe regrowth 225 nm/ well 3 nm	AFM
13	T = 600 °C, SiGe regrowth 225 nm	AFM
14	T = 600 °C, SiGe regrowth 225 nm/well 10 nm	AFM
15	T = 600 °C, SiGe regrowth 225 nm/well 10 nm/ SiGe 50 nm/Si cap 3 nm	AFM, STEM, Raman
16	T = 600 °C, SiGe regrowth 225 nm/well 15nm	AFM
17	T = 600 °C, SiGe regrowth 500 nm	AFM
18	T = 700 °C, SiGe regrowth 5 nm	AFM
19	T = 700 °C, SiGe regrowth 70 nm	AFM
20	T = 700 °C, SiGe regrowth 500 nm	AFM
21	T = 700 °C, SiGe regrowth 225 nm/well 3 nm	AFM
22	T = 700 °C, SiGe regrowth 225 nm/well 15 nm	AFM
23	T = 700 °C, SiGe regrowth 225 nm	AFM
24	T = 700 °C, SiGe regrowth 225 nm/ well 10 nm	AFM
25	T = 700 °C, SiGe regrowth 225 nm/ well 10 nm/SiGe 50 nm/Si cap 3 nm	AFM

Note: The actual Si QW thickness for Wafer #15 is 6.1 nm, as measured with TEM

---

[*] ntjacob@sandia.gov
[†] ebussma@sandia.gov
[‡] Department of Physics, Baylor University, Waco, TX 76798, USA

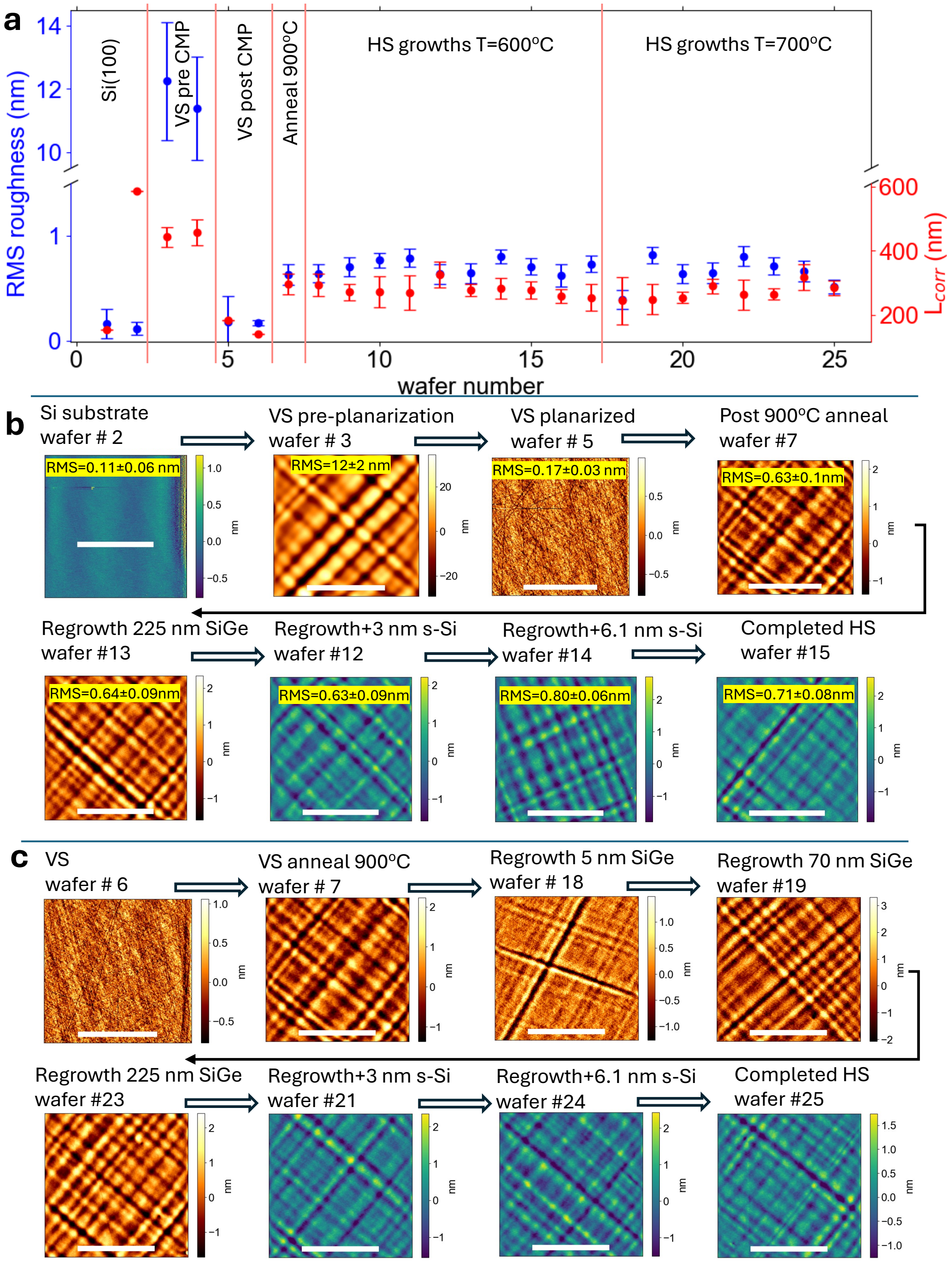

FIG. S1. **Tracking growth surface roughness for the 25 wafer CVD process,** through virtual substrate (VS) preparation, the pre-growth anneal, $T = 900°\text{C}$, and heterostructure (HS) depositions at 600 °C and 700 °C. **a** The calculated root-mean-square (RMS) roughness, and correlation length, L_{corr}, for each wafer with one standard deviation, σ, error bar (among image rows). The L_{corr} error bar is suppressed for clarity for wafers #1, 2, 5, and 6, because it is appreciable owing to difficulty measuring uncorrelated structure of near-atomically flat surfaces. **b** Growth surface evolution at $T = 900°\text{C}$, tracked by AFM imaging after each step. left to right from upper row: Si(100) substrate, relaxed $\text{Si}_{0.7}\text{Ge}_{0.3}$ on graded growth (VS pre CMP), and the VS post CMP surface, and the planarized VS after $T = 900°\text{C}$ pre-growth anneal. Bottom row, left to right: HS growth on epitaxy-ready $\text{Si}_{0.7}\text{Ge}_{0.3}$ VS following regrowth of 225 nm SiGe, then the 3 nm and 6.1 nm s-Si well, and finally the completed HS, after capping the well with 50 nm thick SiGe and 3 nm s-Si. All scale bars 10 μm. **c** Growth surface evolution at 700 °C. These images show that starting from the initially flat VS post CMP (wafers #5 and #6), the pregrowth anneal roughens the surface (RMS $= 0.63 \pm 0.1$ nm) with cross-hatch features, then all subsequent growth steps have comparable crosshatch roughness. That is, roughness is predominately introduced at the anneal (wafer #7), then all subsequent growth process steps do not distinguishably change the roughness and correlation length (wafers #8-25). The roughness stays near 0.6 nm, with three outliers at 0.4 nm and 0.8 nm, while $L_{corr} \sim 300$ nm. Horizontal scale bar is 10 μm.

TABLE S2. Growth temperatures and rates for the various wafers and layers.

Layer	growth T (°C)	Growth rate (nm/min)
Wafers 8-17		
SiGe	600	7
Si	600	0.2
Wafers 18-25		
SiGe	700	75
Si	700	4

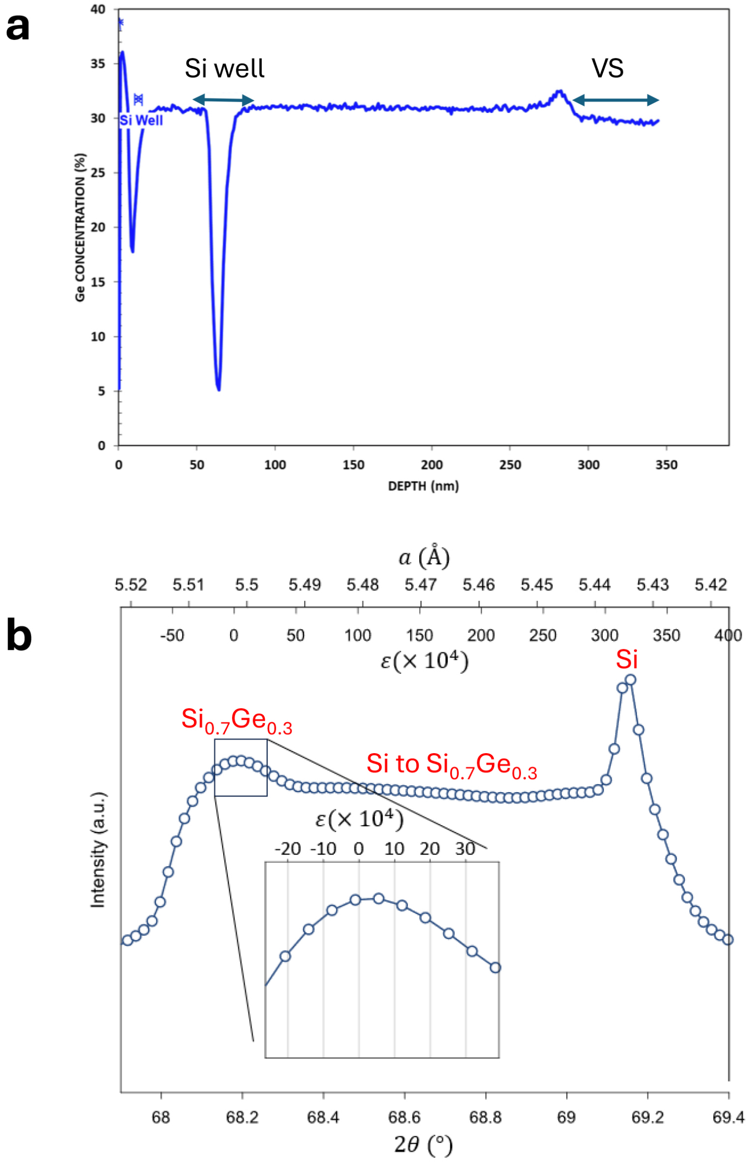

FIG. S2. **Measurements indicating mean composition and elastic state of the of the heterostructure in this study.** **a** Secondary ion mass spectroscopy (SIMS) depth profile indicates the alloy Ge$_x$ content to be $x \sim 0.31$ with a buried Si well at the expected depth ~ 55 nm below the surface, on a ~ 225 nm-thick SiGe buffer atop the virtual substrate (VS). The heterostructure and VS compositions are similar. **b** An X-ray diffraction (XRD) $\omega - 2\theta$ scan (rocking curve) of the heterostructure shows an on average relaxed SiGe thin film on the graded SiGe buffer and Si substrate. The scan was performed on a Rigaku Smartlab X-Ray Diffractometer, and the strain states indicated in the top (below) x-axis were simulated (Rigaku GlobalFit software) for strained and strain-relaxed $Si_{0.7}Ge_{0.3}$. Lattice constants corresponding to the 2θ position are indicated in the top (above) x-axis for reference.

A. Raman imaging

To quantify near-surface strain fluctuations, we performed a strain mapping using Raman microscopy following studies that established a formalism to use Raman modes (Si-Si LO$_z$ shift in the SiGe) to measure the in-plane strain state, $\epsilon_{||}$, in the epitaxial SiGe [1–3]. The essential experimental details are described in the Methods section. Here we explain the analysis in more detail.

Raman measurements reported in the manuscript were obtained using 488 nm light (2.54 eV). Raman strain mapping was performed for several wafers, Fig. S3. Initially, we tried excitation wavelengths 488, 532, and 785 nm. Typical Raman spectra are indicated in Fig S4 a. The 785 nm light probed both the heterostructure and the Si substrate, as indicate by the double peaks around 500 cm^{-1} and 520 cm^{-1}. By contrast, both the 488 nm and 532 nm excitation yield well-defined single-peaked Raman responses consisted with prior studies on SiGe [1–3].

Fig. S4 b shows the average of 5,265 spectra for each sample, characterizing the mean strain state after each process step. The inset highlights a robust and measurable peak shift, significantly exceeding experimental uncertainties. Fig. S4 c-d show typical Raman images plotting the Si-Si peak shift for a virtual substrate following the CMP step. The most salient feature in the images is the familiar crosshatch pattern of strain fluctuations running along (110) directions [4–6]. Several prior works have shown that the Si-Si LO$_z$ peak, ω, in the Si$_{1-x}$Ge$_x$ alloy shifts with composition, x, and strain, $\epsilon_{||}$, by comparable amounts

$$\omega = 520.7 - 66.9x - 730(70)\epsilon_{||}, [1]$$

$$\omega = 520.5 - 62x - 815\epsilon_{||}, [7]$$

$$\omega = 520 - 70.5x - 830\epsilon_{||}, [8], \text{ or}$$

$$\omega = 521 - 62x - 845\epsilon_{||}. [9]$$

For the composition, $x = 0.30 \pm 0.01$, from the SIMS data in Fig. S2 a, we calculate a expected peak position as 500.6 ± 0.7. This is slightly larger than the range (498.5-499.5 cm^{-1}) of measured mean Si-Si peak positions, Fig. S4 f, which is consistent with small average tensile strain ($\epsilon_{||}$ ~1.5-3 $\times 10^{-3}$) in all substrates, Fig. S4 g. In addition, the standard deviations ~0.2 cm^{-1} of the peak distributions for all substrates indicates strain fluctuations on the order of $\delta\epsilon_{||} = 3 \times 10^{-4}$, which is similar to other prior works on comparable materials processes.

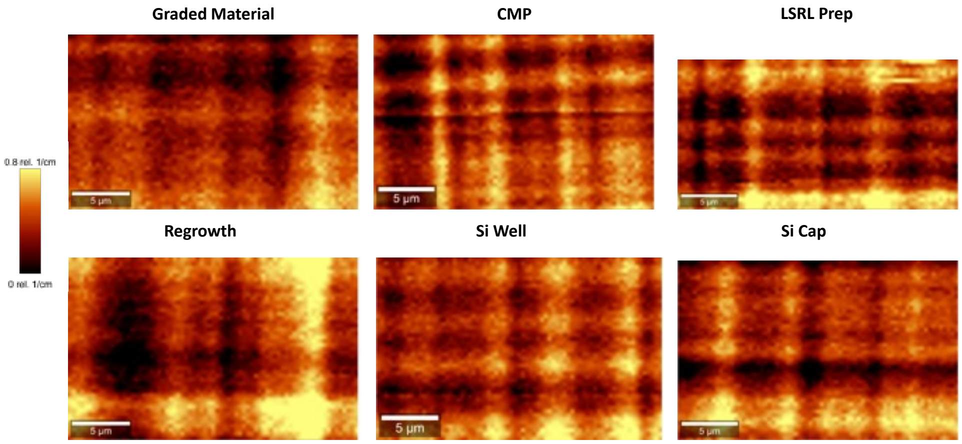

FIG. S3. **To assess near-surface strain variations, Raman microscopy was employed following established formalisms that relate Si–Si vibrational mode shifts in SiGe to the in-plane strain state within the top 200 nm.** Raman images of Si-Si peak position at each process step compared to AFM topographies measured in Fig. S4. Magnitude of range for each image is equivalent (0.8 cm^{-1}).

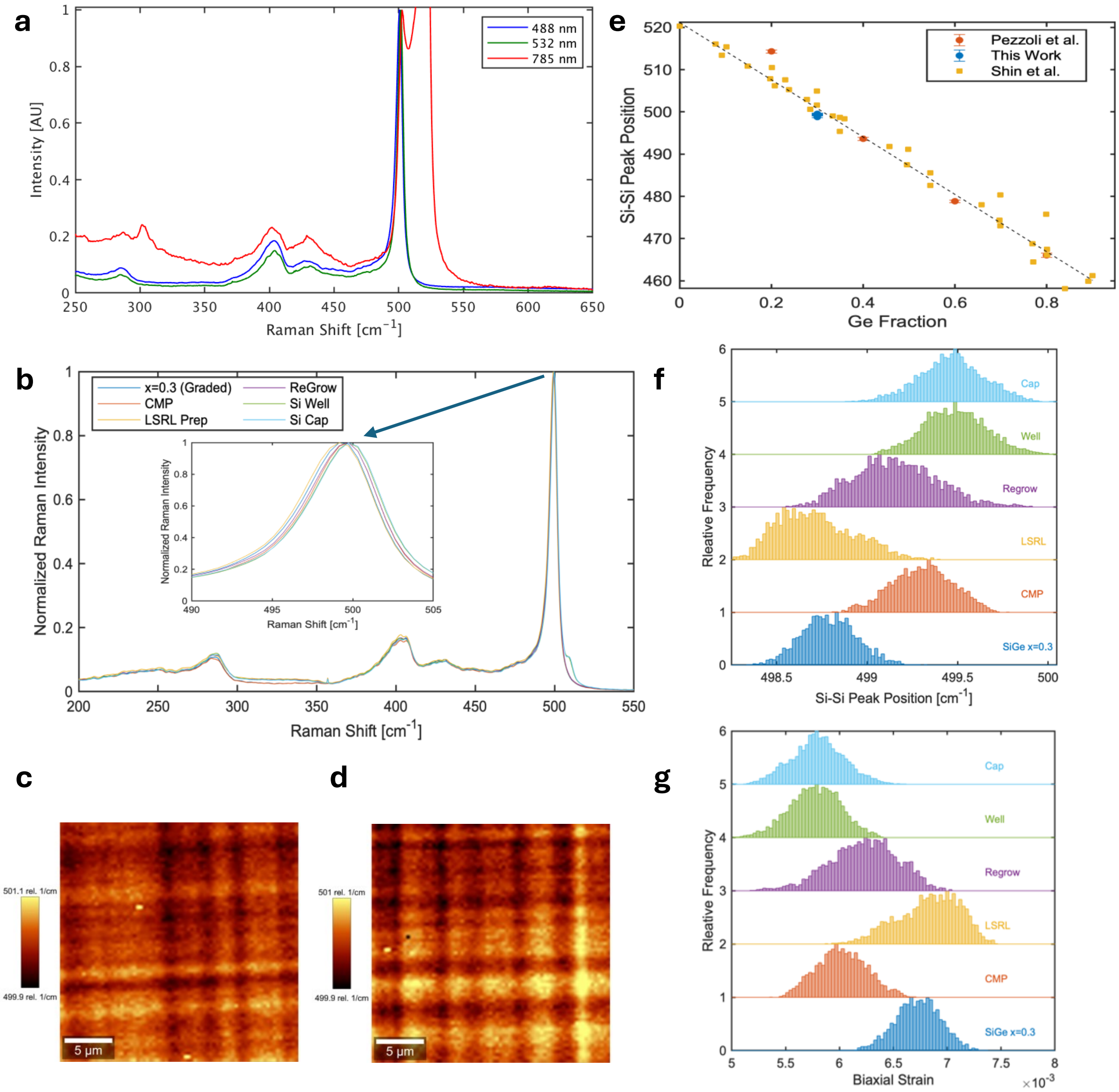

FIG. S4. **Raman-based strain analysis throughout the growth process, correlating Si–Si peak shifts with AFM topographies and highlighting spectral evolution across different stages.** Raman strain analysis of Si-Si peak position to AFM topographies measured in SI Fig. S4. **a** Raman spectra obtained at various wavelengths from a completed polished virtual substrate. **b** Spectra characterizing samples following each stage of the growth process (T = 600 °C). Each curve is the mean normalized spectra across 5625 spectra making up each strain-mapping image. Inset: Zoom-in of Si-Si vibration of SiGe near 500 cm^{-1} where distinct shifting is observed at each step of the process. These shifts are much greater than experimental uncertainties. **c-d** Two examples plots ('Raman' images) of the Si-Si mode's peak position taken with **c** 488 nm and **d** 532 nm laser wavelengths. **e** Our result for Si-Si Raman peak shift plotted alongside data from Shin and Pezzoli [1, 3]. **f** Histograms of Si-Si Raman peak positions over entirety of each dataset for each stage of the growth process. **g** Histograms of strain fluctuations calculated from Si-Si Raman peak positions.

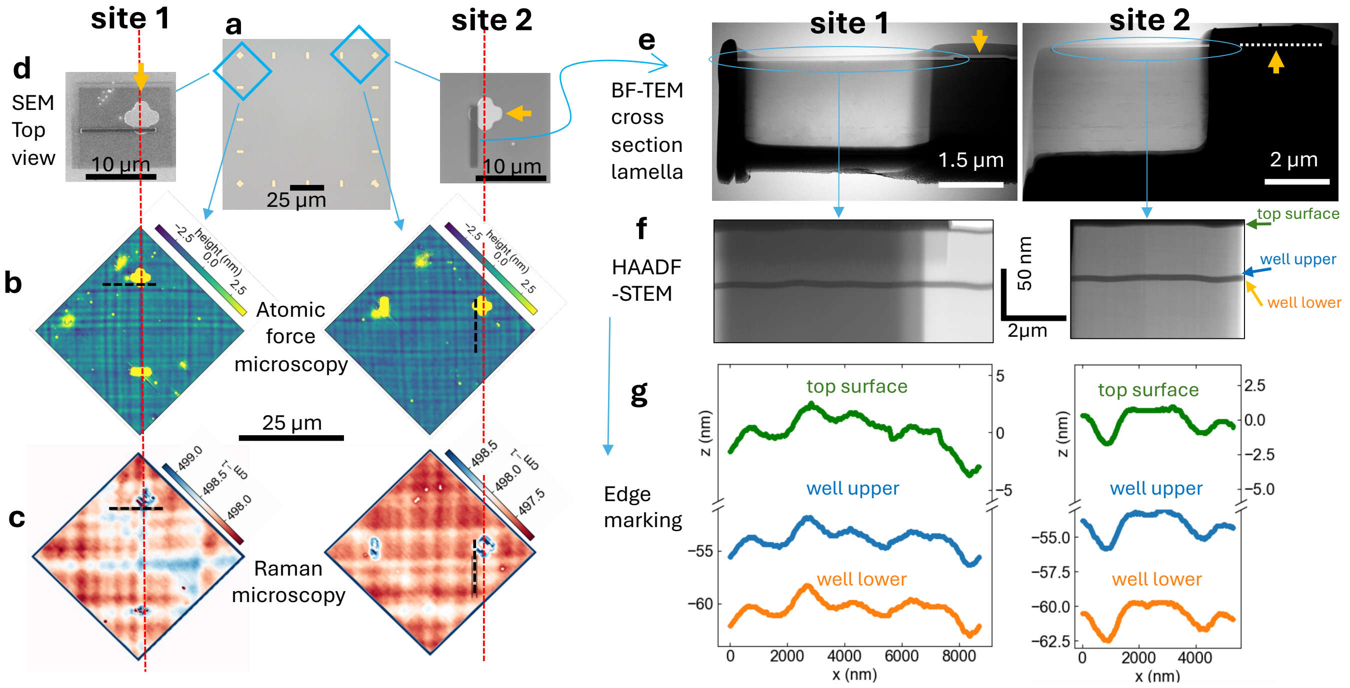

FIG. S5. **Process for spatially-aligned imaging to measure correlations between surface and interface structure, and strain fluctuation.** **a** Metal alignment marks (50 nm-thick Au/ 5 nm-thick Ti) are microfabricated using a liftoff process. Near sites 1 and 2 (blue squares), we perform multi-perspective imaging aligned to '+'-shaped marks. **b** Surface topographies for sites 1 and 2 are measured using atomic force microscopy (AFM) imaging. **c** Next, the near-surface strain variation (Si-Si LO_z phonon shift) is measured using Raman microscopy imaging. Red dashed lines running across the panels indicate the spatial alignment between features. **d** Then cross-sectional lamella are cut-out using standard focused ion beam (FIB) and lift-out techniques. Scanning electron microscopy (SEM) images show the top surface views of the FIB sites (darkest regions). The corresponding location is indicated by black dashed lines in the AFM and Raman images. **e** cross-sectional views of the lamella in bright-field (BF) TEM. Blue ovals indicate the strained-Si well region, orange arrows point out the cross-sectioned metal alignment features location which is verified in cross-sectional SEM imaging with sub-100-nm precision (not shown). **f** High-angle annular dark field scanning transmission electron microscopy images of the quantum well region. Note that vertical axis is exaggerated to 32:1 scale to emphasize the well structure, as indicated by the scale bars. **g** A Canny edge marking is used to mark and plot the top surface and the the s-Si quantum well upper and lower interfaces.

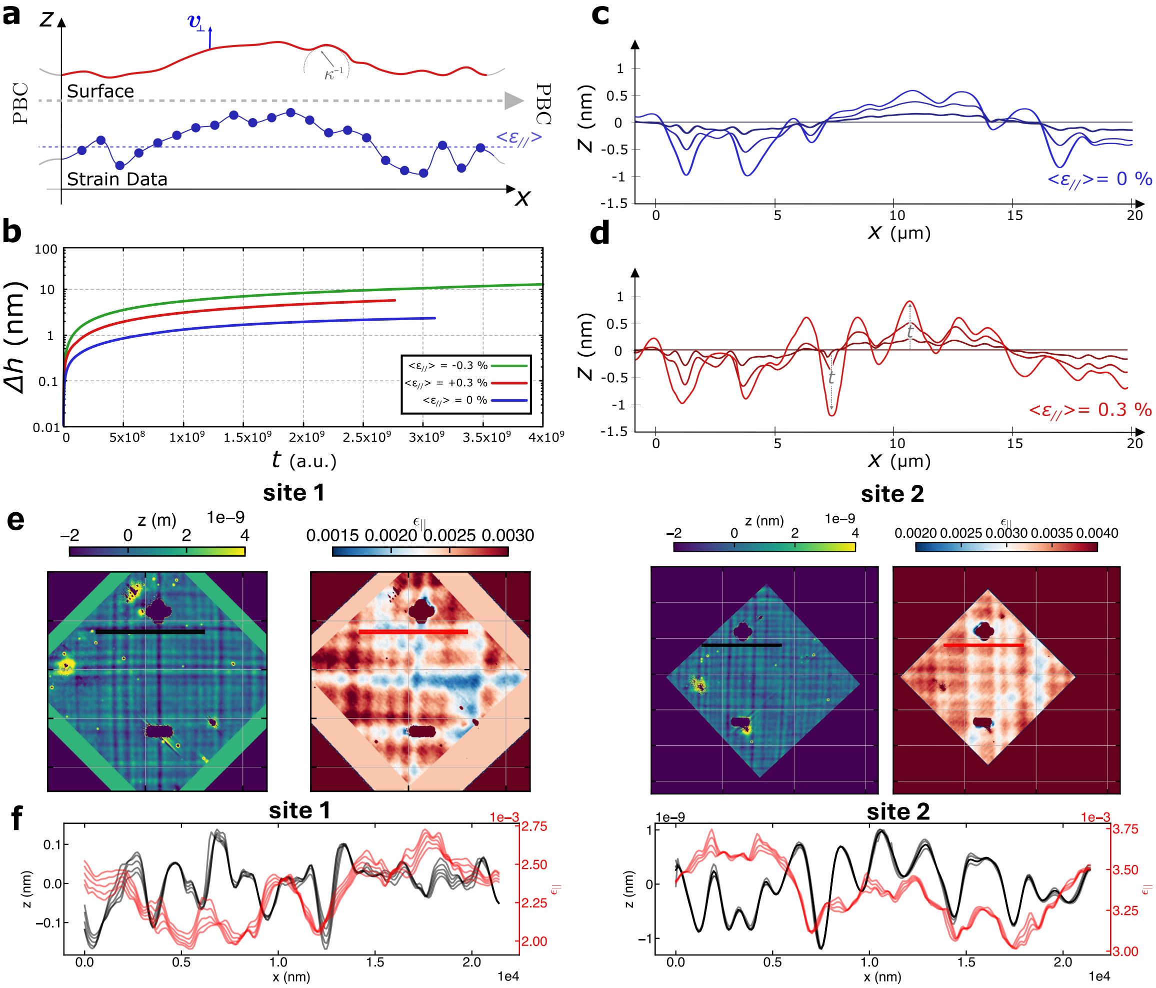

FIG. S6. **The simulation framework and its outcomes, including surface roughness evolution under varying in-plane strain and representative surface profiles at different time steps.** **a** Schematic representation of the model **b** Surface roughness (difference between maximum and minimum of the surface profile) over the simulation time for different values of the average in-plane strain. **c** Snapshots of the surface profiles obtained at different simulation times for the case of $\langle \epsilon_{\|} \rangle = 0\%$. The starting condition at $t = 0$ corresponds to the flat profile. **d** Snapshots of the surface profiles obtained at different simulation times for the case of $\langle \epsilon_{\|} \rangle = 0.3\%$. The starting condition at $t = 0$ corresponds to the flat profile. **e** Site 1 (left) and site 2 (right) AFM an Raman microscopy images showing the locations, indicated by black and red lines of length 21 μm, for **f** the strain, $\epsilon_{\|}$, and topography, z, used in the manuscript Fig. 3. These line are near the sites for cross-sectional HAADF-STEM imaging, just about 2 μm offset to avoid alignment marks.

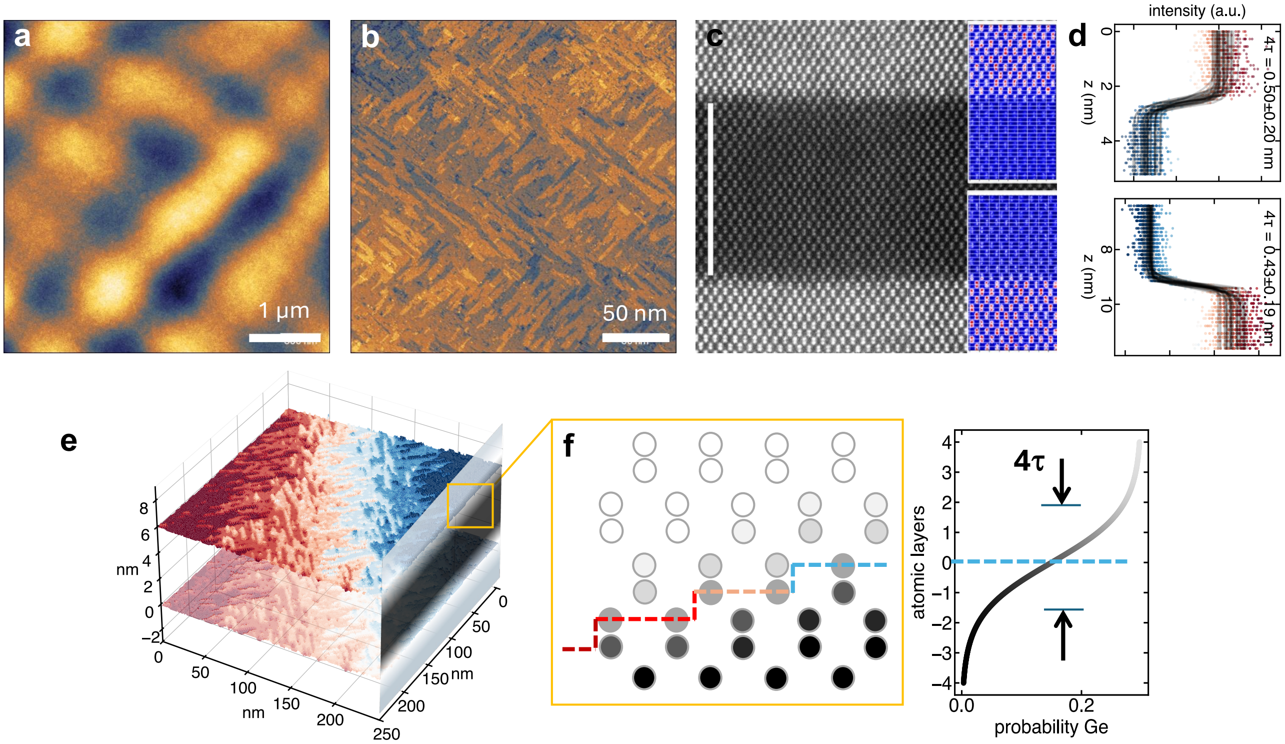

FIG. S7. **The basic ingredients of our atomic structure model used in our calculations of the influence of atomic-step and alloy disorder on valley splitting variability. a** Atomic resolution scanning tunneling microscopy (STM) data showing the cross-hatch surface of the virtual substrate after the pregrowth anneal (wafer #7). **b** Higher-magnification STM showing the cascade of atomic steps on the surface. **c** Quantum well interfaces in a high-angle annular dark field scanning transmission electron microscopy image of a completed heterostructure (wafer #15). The colored insets show the marking of image atomic columns to detect the column intensity, a measure of the composition, in the interface region. **d** The estimation of the interface widths using a sigmoid fit to the column intensity along each atomic plane across the interface. The metric for the interface width is 4τ, where τ is the sigmoid width parameter. We find $4\tau = 0.47 \pm 0.21$ nm. **e** The marked atomic planes in the STM data of a typical sloped region (0.1° local miscut) of the cross-hatch pattern. **f** To compile an atomic structure model of the well-region including both the atomic steps and alloy distribution across each interface, the effective local mean position of each interface is set by the atomic layers marked in the STM data, separated by 6.1 nm well width, then a specific alloy disorder realization (distribution of Ge around each mean local interface center) is calculated as a Bernoulli trial at each atomic site drawing from a sigmoid probability distribution with the width parameter, $4\tau = 0.47 \pm 0.21$ nm, from the HAADF-STEM intensity and the center position at the local layer height from the STM.

[1] F. Pezzoli, E. Bonera, E. Grilli, M. Guzzi, S. Sanguinetti, D. Chrastina, G. Isella, H. von Känel, E. Wintersberger, J. Stangl, and G. Bauer, Phonon strain shift coefficients in $\mathrm{Si}_{1-x}\mathrm{Ge}_x$ alloys, Journal of Applied Physics **103**, 093521 (2008), https://pubs.aip.org/aip/jap/article-pdf/doi/10.1063/1.2913052/15018874/093521_1_online.pdf.

[2] J. M. Baribeau, D. J. Lockwood, and R. L. Headrick, Nature and evolution of interfaces in $\mathrm{Si}/\mathrm{Si}_{1-x}\mathrm{Ge}_x$ superlattices, J. Electron. Mater. **24**, 341 (1995).

[3] H. Shin, D. Lockwood, and J.-M. Baribeau, Strain in coherent-wave sige/si superlattices, Solid State Communications **114**, 505 (2000).

[4] K. Sawano, K. Kawaguchi, S. Koh, Y. Hirose, T. Hattori, K. Nakagawa, and Y. Shiraki, Surface planarization of strain-relaxed sige buffer layers by cmp and post cleaning, Journal of The Electrochemical Society **150**, G376 (2003).

[5] E. Fitzgerald and S. Samavedam, Line, point and surface defect morphology of graded, relaxed GeSi alloys on Si substrates, Thin Solid Films **294**, 3 (1997).

[6] J. W. P. Hsu, E. A. Fitzgerald, Y. H. Xie, P. J. Silverman, and M. J. Cardillo, Surface morphology of relaxed $\mathrm{Ge}_x\mathrm{Si}_{1-x}$ films, Appl. Phys. Lett. **61**, 1293 (1992).

[7] J. Tsang, P. Mooney, F. Dacol, and J. Chu, Measurements of alloy composition and strain in thin ge x si1- x layers, Journal of applied physics **75**, 8098 (1994).

[8] T. Perova, J. Wasyluk, K. Lyutovich, E. Kasper, M. Oehme, K. Rode, and A. Waldron, Composition and strain in thin si1-xgex virtual substrates measured by micro-raman spectroscopy and x-ray diffraction, Journal of applied physics **109** (2011).

[9] D. Rouchon, M. Mermoux, F. Bertin, and J. Hartmann, Germanium content and strain in si1- xgex alloys characterized by raman spectroscopy, Journal of crystal growth **392**, 66 (2014).